Research Square

Preprints are preliminary reports that have not undergone peer review.
They should not be considered conclusive, used to inform clinical practice,
or referenced by the media as validated information.

Investigation of the influence of resin coating and heat treatment on the mechanical properties of topology-optimized parts made of polylactic acid (PLA) by the fused filament fabrication (FFF)

Ali Jadali
Semnan University
Vahid Abedini
v.abedini@semnan.ac.ir

Semnan University
Abdolvahed Kami
Semnan University

Research Article

Keywords: Topology optimization, Fused filament fabrication (FFF), Polylactic acid (PLA), Heat treatment, Resin coating

Posted Date: March 5th, 2026

DOI: https://doi.org/10.21203/rs.3.rs-8917297/v1

License: This work is licensed under a Creative Commons Attribution 4.0 International License.
Read Full License

Additional Declarations: No competing interests reported.

Version of Record: A version of this preprint was published at Progress in Additive Manufacturing on August 4th, 2026. See the published version at https://doi.org/10.1007/s40964-026-01887-2.

Investigation of the influence of resin coating and heat treatment on the mechanical properties of topology-optimized parts made of polylactic acid (PLA) by the fused filament fabrication (FFF)

Keywords:
Topology optimization;
Fused filament fabrication (FFF);
Polylactic acid (PLA);
Heat treatment;
Resin coating

Abstract:
Fused filament fabrication (FFF) allows the manufacturing of complex and lightweight polymer components; yet, the mechanical performance of topology-optimized parts is constrained by interlayer weaknesses, residual stresses, and diminished crystallinity. This study systematically investigates the combined effects of heat treatment and resin coating on the compressive behavior of topology-optimized polylactic acid (PLA+) structures produced by FFF. Topology optimization was conducted utilizing the Solid Isotropic Material with Penalization (SIMP) approach to attain a specified mass reduction of 60% while maintaining structural stiffness. The optimized geometry was manufactured and later subjected to post-processing at various heat-treatment temperatures and durations, both with and without resin coating. A central composite design (CCD) inside a response surface methodology (RSM) framework was utilized to assess the individual and interaction effects of post-processing parameters on the maximum compressive load (MCL). Statistical investigation indicated that heat-treatment duration is the most significant variable, succeeded by temperature and coating condition. An ideal post-processing conditions around 82 °C for 90 minutes with resin coating provided a ~34% increase in MCL relative to the as-printed topology-optimized specimen. X-ray diffraction analysis verified a significant increase in crystallinity (≈232%), explaining the noted mechanical enhancement, whereas FESEM analysis indicated a consistent, defect-free coating layer with robust interfacial adhesion. The suggested combined optimization and post-processing strategy provides an efficient method for manufacturing lightweight PLA components with significantly enhanced load-bearing capacity for engineering applications.

1. Introduction

In recent years, additive manufacturing technology has emerged as a potent approach for manufacturing parts with complex and optimized geometry, [1].. This technique, utilizing 3D data, allows the layer-by-layer manufacturing of components with distinctive characteristics, such as weight reduction, enhanced performance, and extensive modification [2, 3]. The Fused Filament Fabrication (FFF) or Fused Deposition Modeling (FDM) process is regarded as one of the most common additive manufacturing techniques for generating polymer components, owing to its accessibility, affordability, and capability to treat thermoplastic materials, [1, 2]. This method involves feeding the filament through a heated nozzle, where it melts and is subsequently deposited onto the printing platform. The mechanical properties of components fabricated using FFF are influenced by several parameters, including nozzle temperature, printing speed, layer thickness, filling pattern, and interlayer adhesion, [4]. Nonetheless, components manufactured by this technique typically exhibit porosity, interlayer discontinuities, and inferior strength compared to those produced by conventional processes, such as plastic injection molding. Consequently, post-processing techniques such as heat treatment and resin coating have been implemented as effective means to enhance the mechanical properties of FFF components, [5, 6]. Resin coating can augment surface adhesion, diminish porosity, and enhance the mechanical properties of the component, [7]. Conversely, heat treatment (annealing) is a thermal procedure wherein the component is heated to a temperature that lies between the glass transition temperature and the melting temperature, followed by a controlled cooling process after maintaining the temperature for a specified duration. This method significantly enhances the mechanical properties of polymer components by enhancing crystallinity, diminishing residual stresses, and boosting elastic characteristics, [8, 9]. With the progression of 3D printing technology, topology optimization has emerged as an effective design methodology for creating lightweight, efficient structures with optimal material allocation. Numerous techniques, including Solid Isotropic Material with Penalization (SIMP), Evolutionary Structural

Optimization (ESO), and Bi-directional Evolutionary Structural Optimization (BESO), have been introduced to derive optimal geometries that facilitate the design of high-performance components with reduced material usage, [10-18]. Nonetheless, the intricate geometry of topology-optimized components is typically achievable solely through additive manufacturing techniques; however, the existence of slender sections, intricate designs, and stress concentrations in these components renders their mechanical performance significantly reliant on manufacturing quality and interlayer characteristics [19]. Numerous research has examined the influence of printing and post-processing factors on the mechanical properties of FFF polymer components. For instance, Fu et al. [20], enhanced the SIMP approach and utilized suitable filters to yield dependable results in optimized components. Dvorakova and Dvorak [21], demonstrated that the production of optimized components via FFF is viable, albeit the intricate geometry of certain pieces elevates machining costs in conventional methods. Antar et al. [22], documented a 30% reduction in volume for an improved bracket utilizing ABAQUS software. Moreover, numerous research have examined the influence of printing factors, including printing direction, speed, filling pattern, filling density, layer thickness, and nozzle temperature, on the tensile, compressive, and flexural properties of PLA and ABS samples, [23-34]. Numerous research indicate that increasing filling density, optimizing layer thickness, and choosing the suitable filling pattern can enhance mechanical strength, [24-26]. The impact of heat treatment on enhancing crystallinity, diminishing porosity, and enhancing tensile and flexural strength of PLA components has been thoroughly investigated, [5, 35-41]. Yu et al. [40], examined the influence of annealing on the flexural strength, crystallinity, and dimensional alterations of PLA samples fabricated using FFF technology. The researchers examined the crystallinity of the samples by X-ray diffraction (XRD) and differential scanning calorimetry (DSC). The flexural strength was assessed with a bending test apparatus in accordance with ASTM D790-17. Their data indicate that annealing enhances the crystallinity of PLA. The optimal temperature range for this process is between the glass transition temperature and the crystallization temperature, stated to be within 65 to 110 °C. Janmanee and Ratchapakdee [41], examined the tensile strength of PLA utilizing the analysis of variance (ANOVA) method, incorporating three temperature levels and two annealing time levels. They discovered that elevating the process temperature and extending the duration both led to higher tensile strength. This effect was attributed to the enhancement of the material's crystallinity with the use of PLA annealing heat treatment. Research has also been undertaken in the domain of coatings. Barone et al. [42] shown that acrylic and epoxy resin coatings can enhance the tensile strength of FFF samples. López Taborda [7] and Koçak [43] similarly demonstrated enhancements in impact strength and mechanical properties upon coating. Additional research has examined the impact of metallic, composite, and hydrophobic coatings on the mechanical and surface properties of samples [44, 45]. Chiocca et al. [46], examined the influence of photopolymer coatings on the fatigue life and tensile strength of a PLA network structure fabricated by FFF. To fabricate the coating, scientists immersed the sample in a photopolymer tank and subsequently cured it using ultraviolet light. This type of coating resulted in a 21% enhancement in strength and a 9% reduction in elongation at break. Nevertheless, limited research has assessed the impact of concurrent heat treatment and resin coating on topologically optimized components. This is particularly significant since topological structures are more reliant on reinforcement techniques than other components due to the existence of restricted width areas and heightened sensitivity to interlayer discontinuities.

This study's novelty is in the concurrent use of heat treatment and resin coating to enhance the mechanical properties of PLA samples, which have been optimized for topology using the SIMP approach and manufactured by FFF. This study examined the influence of heat treatment temperature and duration, together with resin coating, on the compressive behavior of samples, employing the statistical method of central composite design (CCD), a form of response surface methodology (RSM). This method enhances strength, diminishes mass, and improves the manufacturing capacity of topological components, facilitating the creation of lightweight and efficient structures in engineering applications.

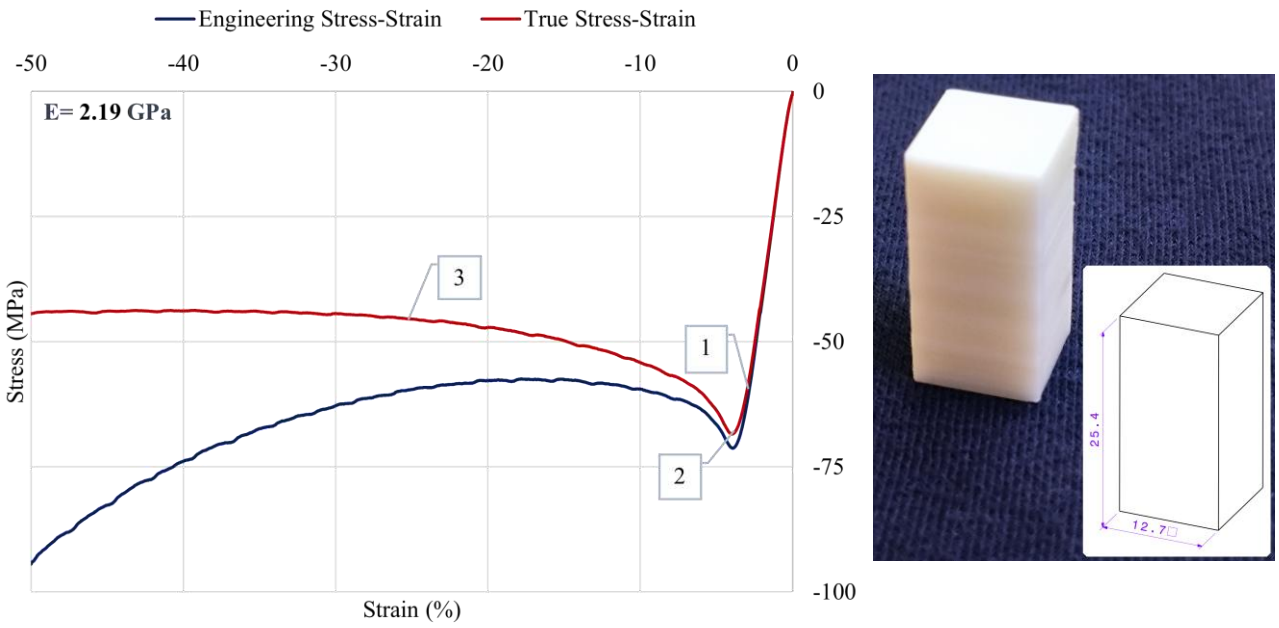
2. Materials and Methods

2.1. Specimen Preparation

The preparation of topology-optimized specimens includes six phases, detailed as follows:

- Step 1: Conducting a compression test using a standard specimen to obtain the mechanical properties of PLA+
- Step 2: Conducting the compression test simulation for convergence and mesh independence
- Step 3: Topology Optimization
- Step 4: Redesigning the geometry derived from the topology optimization process
- Step 5: Conducting the compression test simulation with the topology-optimized specimen
- Step 6: Designing the support structure and manufacturing specimens

Step 1: The standard specimen was designed utilizing CATIA 2022 software in accordance with the ASTM D695 standard to attain PLA+ mechanical properties, and subsequently transformed into a layer-by-layer file for 3D-printing with Simplify3D V4.1.2 software. Next, it involved preparing the output G-Code file from the program and transmitting it to the 3D printer via Pronterface V2.0.1, followed by the execution of the specimen printing process, as illustrated in Fig. 1. The compression test was conducted on the standard specimen to a strain of 50%. Fig. 1, displays the stress-strain diagram alongside the Young's modulus value. Fig. 1, indicates that the elastic region of PLA+ exists within the strain range of 0 to 4%. Consequently, a strain range of 0 to 3% was employed to optimize the topology in ABAQUS software. To attain the ideal element size and execute the convergence process while ensuring mesh independence, the real stress-strain diagram was utilized within the strain range of 0 to 25%.



No.	Goal
1.	Topology Optimization
2.	Identification of Yield Strength and Elastic Region
3.	Compression Test Simulation, Convergence and Mesh Independence

Fig. 1 Stress-strain diagram of a standard specimen exhibiting up to 50% strain, inclusive of Young's modulus.

Step 2: The conditions for the compression test simulation regarding convergence and mesh independence are as follows:

Modeling: In ABAQUS software, the component model was designated as deformable as illustrated in Fig. 2. Two square flat plates measuring 30×30 mm were utilized as hard components to delineate the jaws of the compression apparatus. Each plate associated with the device was partitioned into four pieces, while the sample was segmented into nine sections to delineate nodal lines for the measurement of the applied load, as illustrated in Fig. 2 (a).

Material: The data pertaining to Fig. 1 and Table 1 were utilized to delineate the specimen material (PLA+) in the simulation. The characteristics utilized for material behavior in ABAQUS software encompass density, Young's modulus, and the range of plastic deformation.

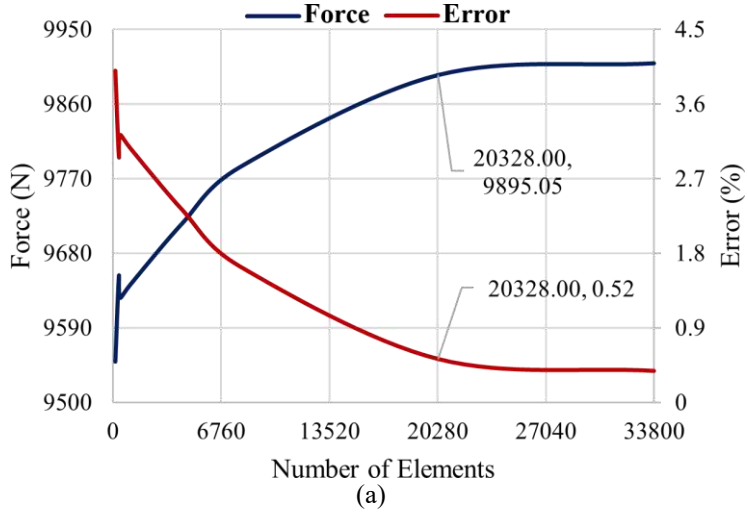
Interaction: An interaction was established with a contact constraint featuring a friction coefficient of 0.3 between the force application plates and the sample.

Load: One of the force planes was restricted in both directions, and a displacement constraint of 6.35 mm (25% strain) was established for the force plane along the Z axis. The force plane was restricted in the other directions, as illustrated in Fig. 2(a).

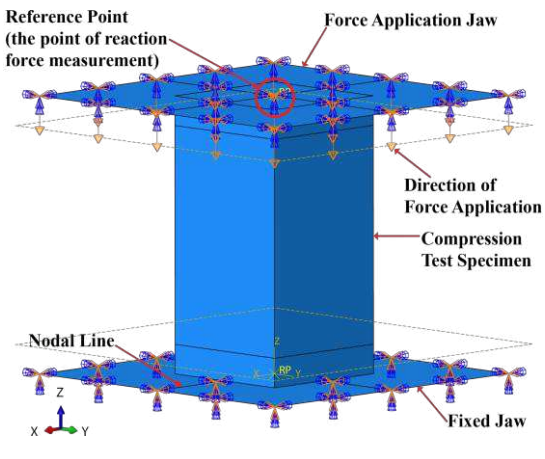
Element: The element size was altered from 3 mm to 0.5 mm to facilitate the convergence and mesh independence process. The element type C3D8R was chosen in all phases. The C3D8R is an eight-node, linear, continuum, hexahedral with reduced integration, and general-purpose finite element. The mesh control was configured to a hex structured pattern.

Reference point: The reaction force was measured at the reference point of the force plane to conduct the convergence and mesh independence process as illustrated in Fig. 2(a).

Figure 2(b), presents the findings of the convergence and mesh independence analysis. At an element size of 0.6 mm, the deviation from the experimental data has fallen below 1%, which is deemed an acceptable level of accuracy for the simulation process. The figure illustrates that the force variations during the simulation process originally fluctuated significantly but began to stabilize from a mesh size of 1 mm onward, suggesting an enhancement in the accuracy of the simulation findings. The error variation depicted in this graph pertains to the acceptable error threshold (≤1%) for element sizes of 0.5 and 0.6 mm. The results from the convergence and mesh independence analysis indicated that an element size of 0.6 was utilized for the topology optimization process. The reason for not selecting an element size of 0.5 mm, despite its lower error value, is the decrease in volume and computational time.



(a)



(b)

Element Size	Number of Nodes	Number of Elements	Elements Type	Reaction Force (N)		Variation (%)	Error (%)
				Theoretical	Experimental		
3	250	144	C3D8R	9776.95	9947.00	-------	1.71
2.5	539	360		9707.97		0.71	2.40
2	637	432		9701.54		0.07	2.47
1.5	1458	1088		9696.18		0.06	2.52
1	5292	4394		9716.08		0.21	2.32
0.8	9248	7936		9794.22		0.80	1.54
0.6	22747	20328		9878.13		0.86	0.69
0.5	37179	33800		9934.49		0.57	0.13

Fig. 2 (a) Conditions for compression test simulation, (b) results of convergence and mesh independence study

Step 3: The configurations for the compression test simulation used for topology optimization are similar to those in Step 1. The distinctions encompass the following:

Modeling: The compression test specimen was segmented into 12 parts to establish nodal lines, facilitating the delineation of optimization conditions, as illustrated in Fig. 3(a).

Material: The parameters utilized for the material behavior in ABAQUS software encompass density and Young's modulus.

Load: A displacement constraint of 0.7631 mm (3% strain) was established along the Z axis for the force application plane, as illustrated in Fig. 3(a).

Element: The element size was specified as 0.6 mm.

The specified optimization conditions are as follows:

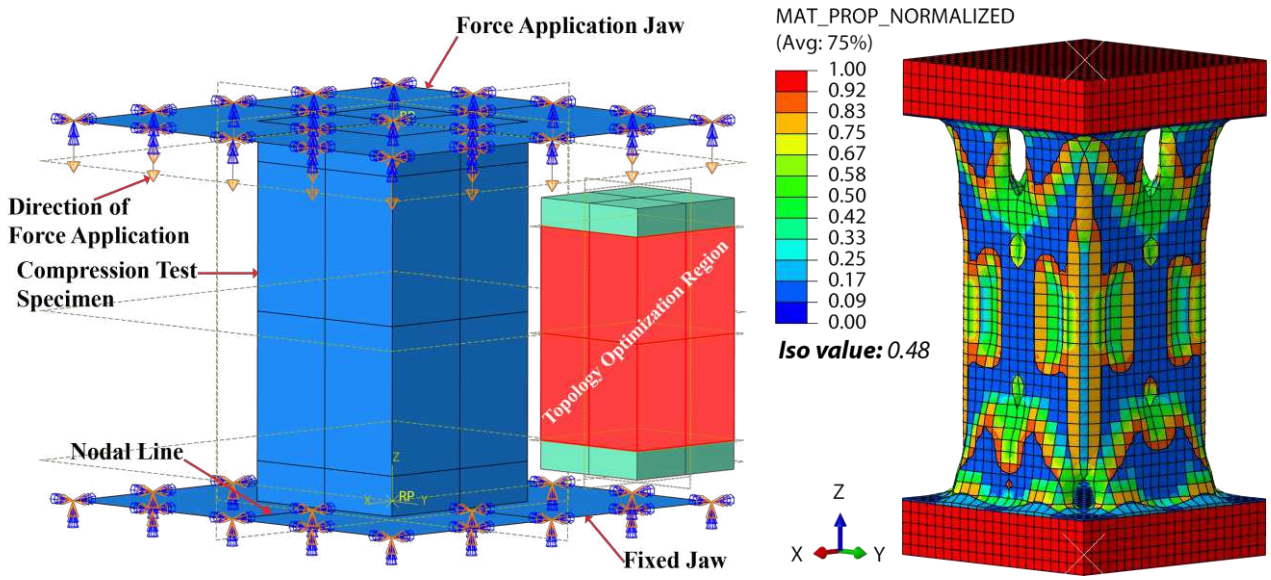
Optimization region: The topology optimization region encompasses the central 20 mm segment of the compression test specimen, as seen in Fig. 3(a).

Objective: Maximize stiffness while achieving a 60% reduction in mass.

Geometric constraints: 1- In the additive manufacturing process, overhangs exceeding a 45-degree angle relative to the building axis require support for printing; thus, a geometric constraint limiting the overhang angle to 45 degrees relative to the Z axis was imposed on the specimen. 2- A plane symmetry constraint was established using a vector perpendicular to the Z axis.

Topology optimization method: The SIMP method was chosen for the topology optimization of the compression test specimen, utilizing a penalty factor of 3.

Figure 3(b), presents the distribution contour of the normalized relative material density of the optimized structure. This parameter was used to represent the spatial distribution of material during the topology optimization process. The red regions correspond to areas of high relative density, indicating critical load-bearing zones where material removal is restricted due to structural stiffness and integrity requirements. Material elimination is permitted only in regions where the overall structural performance is not adversely affected.



(a) (b)

Fig. 3 (a) Conditions for compression test simulation intended for topology optimization, (b) distribution contour of the normalized relative material density

Step 4: The raw geometry derived from the topology optimization process is not directly suitable for printing due to surface imperfections and jagged features. Furthermore, the optimization output yields only triangulated surface data instead of a manufacturable CAD model. Consequently, a geometry reconstruction phase was executed to refine the surfaces and provide a printable solid model. The redesign process is using CATIA 2022 to improve the optimal geometry and then convert it into a CAD model appropriate for additive manufacturing. All geometries included in the following simulations were derived from the reconstructed and optimized models at this stage.

Step 5: The existence of surfaces perpendicular to the construction plate necessitated the incorporation of supplementary support structures, especially in the middle area of the specimen. A cylindrical hole with a diameter of 2.85 mm was integrated into the upper section of the model to reduce the volume of necessary supports. A specialized support-blocking geometry was created to inhibit the generation of support material on the lower surface of the component. Fig. 4, depicts the support-control features and the final printed shape of the specimens. All samples were manufactured utilizing shared geometry and the processing settings specified in Table 1.

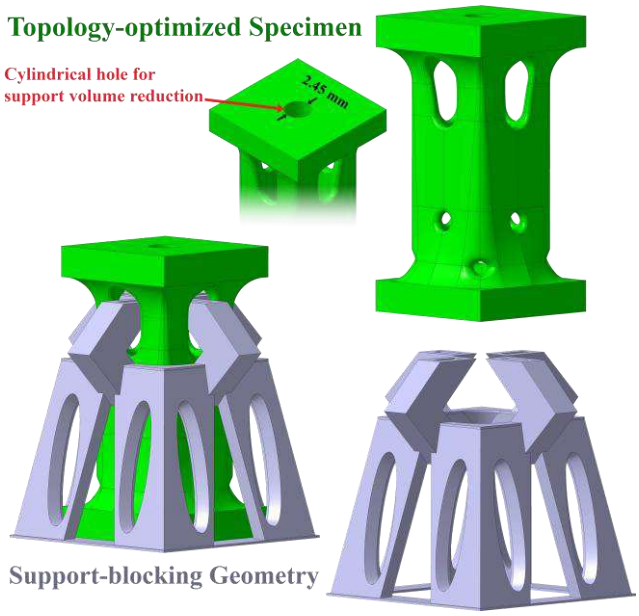


Fig. 4 Support-blocking geometry and final printable geometry of the specimens

Step 6: A compression test simulation was conducted on the redesigned topology-optimized specimen, according to the similar boundary conditions and loading procedure outlined in Step 3. The only other difference was the element formulation: a quadratic ten-node tetrahedral element (C3D10) was utilized. A free tetrahedral meshing strategy was implemented. To ensure a consistent comparison between the standard and topology-optimized geometries, the maximum von Mises stress was assessed at a cross-section positioned at X = 4.04 mm and under a global compressive strain of 3%. Fig. 5, illustrates that the disparity in the maximum von Mises stress between the two specimens is negligible. The results demonstrate that the topology-optimized design attains a reduction in mass while preserving a similar load-bearing capacity and strength.

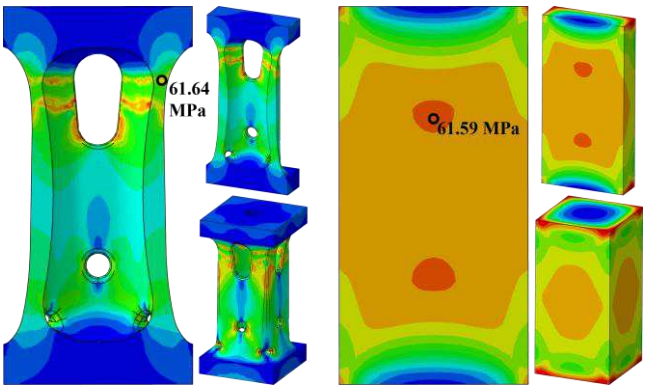


Fig. 5 Comparison of von Mises stress distribution in two specimens with and without topology optimization at 3% strain in cross-section X=4.04mm

Figure 6, presents a comparison between the images from the experimental compression tests and the corresponding results from finite element analysis (FEA) across the strain range of 0–25%. A strong correlation between the simulated and experimental deformation patterns is seen, demonstrating that the numerical model accurately reflects the compressive behavior of the topology-optimized specimen.

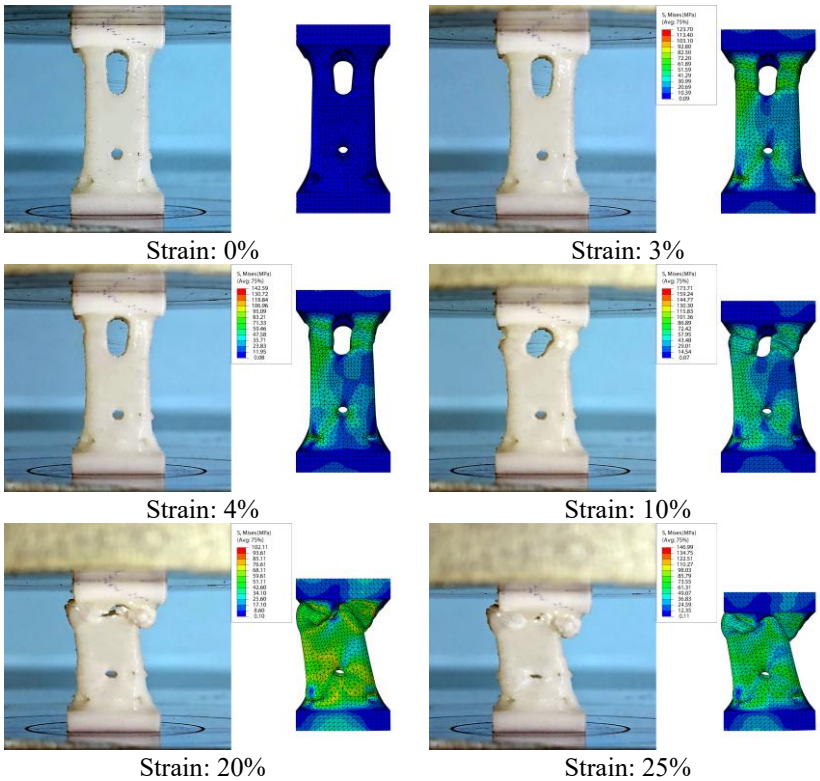


Fig. 6 Comparison of deformation obtained from experimental compression test and FEA for topology-optimized specimens

2.2. Material and Equipment

A white PLA+ filament (diameter: 1.75 mm) manufactured by eSUN (China) was utilized for specimen manufacturing. The filament specifications are delineated in Table 1. All specimens were manufactured on a Sizan 4 desktop version 3D printer employing the FFF method. The printing parameters were chosen based on the printer characteristics and the filament manufacturer's datasheet, as detailed in Table 1.

Table 1 Material properties of eSUN PLA+ filament and operational parameters of the FFF process [47, 48]

Physical Property	**Unit**	**Value**
Density	g/cm^3	1.23
Melt Flow Index	$g/10min$	5
Melting Temperature	$°C$	150-180
Poisson's ratio	-----	0.35
FFF Operational Parameter	**Unit**	**Value**
Extruder Temperature	$°C$	220
Bed Temperature	$°C$	55
Print Speed	mm/min	2400
Nozzle Diameter	mm	0.4
Layer Thickness	mm	0.2
Number of Outline Solid Layer	-------	3
Infill Percentage	%	100
Fan Speed	%	30

This study utilized a standard gray photopolymer resin manufactured by Anycubic (China) as the coating material. The resin's physical properties and post-processing parameters, as detailed in the manufacturer's datasheet, are encapsulated in Table 2. A "Do It Yourself (DIY)" ultraviolet (UV) curing machine was used for the coating process. The equipment featured two primary functions: regulated UV irradiation and a rotating platform, Fig. 7.

The specimens were immersed in 300 mL of resin for 15 minutes and then positioned in the UV curing machine. UV irradiation was administered for 15 minutes at a wavelength of 400 nm to cure the coated layer. Subsequent to UV treatment, the samples were subjected to a 3-minute soak in alcohol to eliminate excess and uncured resin.

Table 2 Physical and mechanical properties of Anycubic standard resin and post-processing conditions, [49]

Physical and Mechanical Property	**Unit**	**Value**
Viscosity	$mPa \cdot s$	250-350
Density	g/cm^3	1.05-1.25
Hardness	$Shore\ D$	80-83
Tensile Strength	MPa	35-45
Elongation at Break	%	25-30
Bending Modulus	MPa	40-50
Bending Strength	MPa	1500-2100
Izod Impact Strength	J/m	102
Volume Shrinkage Rate	%	4.3-5.6
Post-processing Condition		
Wavelength required for solidification	nm	365-405
Curing time in UV curing machine	min	≥3
Alcohol soak time	min	≥3



Fig. 7 UV Curing Machine

The heat treatment was conducted in a low-temperature furnace with a temperature control precision of ±2 °C and a maximum operational temperature of 350 °C. The furnace chamber was insulated with glass wool to reduce heat loss to the surrounding environment. Compression tests were performed utilizing an STM-400 universal testing equipment (SANTAM, Iran). The loading rate was established at 1.3 mm/min in accordance with ASTM D695. The testing machine's compression platens were utilized to exert the load.

The phase transition temperatures were determined employing a DSC-400 differential scanning calorimeter (Sanaf, Iran). The thermal analysis of the 3D-printed PLA+ specimens indicated a glass transition temperature (T_g) of 74.15 °C, a crystallization temperature (T_c) of 110.25 °C, and a melting temperature (T_m) of 185 °C. Consequent to these findings, the heat-treatment temperature range was established between 60 and 130 °C to methodically examine its influence on material behavior.

2.3. Design of Experiment (DOE)

A CCD was employed inside the RSM framework, utilizing Design-Expert 13 software, to optimize post-processing parameters aimed at increasing mechanical strength. Three factors were evaluated as input variables: two numeric factors (heat-treatment temperature and duration) and one categorical factor (Coating). Five levels were designated for the numeric factors, while two levels were established for the categorical factor. The factors and their respective levels are presented in Table 3. The quantity of replicated runs at the center point was established at three, and the alpha value was set as 1.4.

The temperature levels were established based on the DSC data presented in Section 2.2, whereas the heat-treatment time values were chosen in accordance with prior published studies.

Table 3 Input variables of design of experiment along with their values

Parameter		Unit	Value
Heat treatment	Temperature	$°C$	60-70-95-120-130
	Time	min	18-30-60-90-102
Coating		-----	Coated and Uncoated

3. Results & Discussion

According to the DOE, twenty-four PLA+ specimens featuring topology-optimized geometry were manufactured with the FFF method and subsequently post-processed. Following that, each specimen underwent compression testing, and the resultant force–displacement curves were recorded. The maximum sustainable load for every specimen was derived from the curve and reported as the maximum compressive load (MCL), [50]. Table 4, shows the MCL of each specimen.

Table 4 Results of compression tests on the topology-optimized specimens subjected to various post-processing conditions, including heat treatment and coating.

Row	Designation	Heat Treatment	Coating	MCL (N)

		Time (min)	Temperature (°C)		
1	Ti90Te120U	90	120		2017
2	Ti60Te95U (1)	60	95		2541
3	Ti60Te130U	60	130		1334
4	Ti60Te95U (2)	60	95		2418
5	Ti60Te95U (3)	60	95		2296
6	Ti30Te120U	30	120	Coated	1452
7	Ti30Te70U	30	70		1373
8	Ti60Te60U	60	60		1844
9	Ti90Te70U	90	70		2541
10	Ti18Te95U	18	95		1511
11	Ti102Te95U	102	95		2482
12	TiXXTeXXU	--------	--------		1834
13	Ti102Te95C	102	95		2874
14	Ti90Te70C	90	70		2630
15	Ti60Te60C	60	60		1668
16	Ti60Te130C	60	130		1542
17	Ti18Te95C	18	95		1354
18	Ti60Te95C (1)	60	95	Uncoated	2090
19	Ti60Te95C (2)	60	95		1979
20	Ti60Te95C (3)	60	95		1933
21	Ti90Te120C	90	120		2364
22	Ti30Te120C	30	120		1515
23	Ti30Te70C	30	70		1425
24	TiXXTeXXC	--------	--------		1903

Fit statistics play a critical role in evaluating the adequacy and predictive capability of statistical models in experimental design and response surface methodology. These metrics assess how well the proposed model represents the experimental data and help to identify potential sources of bias or lack of fit [51, 52]. In this study, several goodness-of-fit criteria were considered. The coefficient of determination (R^2) and the adjusted coefficient of determination (adjusted R^2) were required to exceed 90%, while the adequate precision value was considered acceptable when greater than 4, [53].

3.1. Statistical Analysis

Externally studentized residuals help to examine the appropriateness of regression models by evaluating the impact of individual data. The residuals are computed by temporarily excluding each observation from the model and calculating the variance in the absence of that data point. The standardized difference between the observed and expected values is later calculated via this externally estimated variance. This method facilitates the detection of outliers and important data points that could negatively impact the robustness and predictive accuracy of the regression model, [54, 55].

3.1.1. Diagnostics plots

Figure 8(a), presents the normal probability plot of the residuals. The data points closely follow a straight line, indicating that the residuals are approximately normally distributed and that no significant outliers are present in the experimental compression test results. Fig. 8(b), shows the externally studentized residuals as a function of the test number. The absence of a systematic trend or structured pattern suggests that the residuals are independent of the experimental sequence and that no time-related bias affected the test results.

Figure 8(c), compares the model-predicted values with the experimentally measured data. The maximum relative error was 9.21% for coated specimens and 5.74% for uncoated specimens. Since the

prediction errors remain below 10%, the developed model can be considered to provide an acceptable level of predictive accuracy.

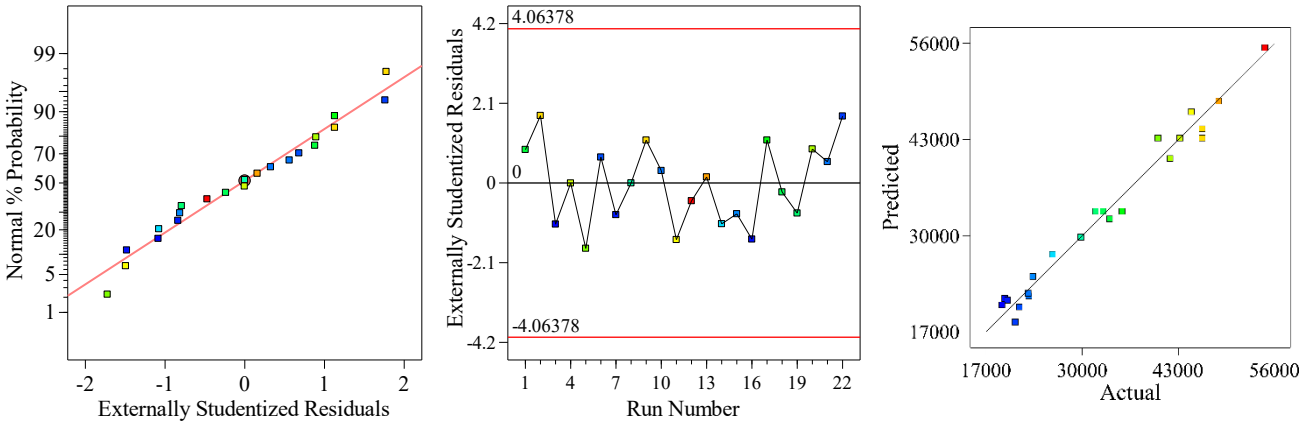


Fig. 8 Essential plots to evaluate the model's suitability

3.1.2. MCL Model

Table 5, presents the outcomes of the analysis of variance (ANOVA) and the fit statistics for MCL response.

Table 5 Results of ANOVA and Fit Statistics for MCL

ANOVA						
	Sum of Squares	**df**	**Mean Square**	**F-value**	**p-value**	**Contribution (%)**	
Model	2.573×10^{9}	10	2.573×10^{8}	49.22	<0.0001	97.80	significant
A-Time	1.727×10^{9}	1	1.727×10^{9}	330.31	<0.0001	65.64	
B-Temperature	7.452×10^{7}	1	7.452×10^{7}	14.26	0.0031	2.83	
C-Coating	1.472×10^{8}	1	1.472×10^{8}	28.16	0.0002	5.59	
AB	6.350×10^{7}	1	6.350×10^{7}	12.15	0.0051	2.41	
AC	4.421×10^{7}	1	4.421×10^{7}	8.46	0.0142	1.68	
BC	1.918×10^{7}	1	1.918×10^{7}	3.67	0.0818	0.73	
A^2	9.010×10^{6}	1	9.010×10^{6}	1.72	0.2160	0.34	
B^2	4.574×10^{8}	1	4.574×10^{8}	87.49	<0.0001	17.39	
A^2C	1.378×10^{8}	1	1.378×10^{8}	26.36	0.0003	5.24	
B^2C	8.143×10^{7}	1	8.143×10^{7}	15.58	0.0023	3.10	
Residual	5.750×10^{7}	11	5.228×10^{6}			2.19	

Lack of Fit	3.272×10^{7}	7	4.674×10^{6}	0.7543	0.6514	1.24	not significant
Pure Error	2.479×10^{7}	4	6.196×10^{6}			0.94	
Cor Total	2.631×10^{9}	21					
Fit statistics	R^2= 97.81% || Adjusted R^2= 95.83% || Predicted R^2= 90.23% || Adequate Precision= 22.9322						

As summarized in Table 5, the selected regression model exhibits a high level of predictive capability for MCL, with an adjusted R^2 exceeding 95%. All three main factors—heat treatment time, temperature, and resin coating—were statistically significant, with p-values less than 0.05. In addition, their interaction effects, as well as the square terms for time and temperature, were also statistically significant.

The contribution percentage of each factor to the model response was 65.98% for heat treatment time, 20.22% for temperature, and 5.59% for resin coating, indicating that heat treatment time is the most influential parameter. The square term for time also showed statistical not significance. However, because of its significant interaction with the coating factor, this term was retained in the final model. The reported contribution percentage were calculated by summing the linear and quadratic effects of each variable.

According to the statistical analysis and the identified relevant terms, the prediction model for the MCL of the topology-optimized specimens is articulated as follows:

$$MCL_{\text{Coated}} = (-51585.98073 + 409.18072t + 1316.11173T - 3.75644Tt + 2.92834t^2 - 5.96561T^2)^{\frac{1}{1.37}} \quad (1)$$

%Error= 9.21%

$$MCL_{\text{Uncoated}} = (-1.33567\times10^{5} + 1242.02928t + 2882.93457T - 3.75644Tt - 4.94020t^2 - 14.67541T^2)^{\frac{1}{1.37}} \quad (2)$$

%Error= 5.74%

t: Time
T: Temperature

3.1.3. Parametric influence on the response variable

For investigating the effects of the input variables, three forms of graphical analysis were utilized: perturbation plots, three-dimensional response surface plots, and interaction plots. In perturbation plots, a greater slope or pronounced curvature signifies a more substantial impact of a factor on the response. Figs. 9(a) and 9(b), illustrate the perturbation plots. These findings demonstrate that both numeric variables considerably impact the response; however, the effect of temperature is less obvious in the coated specimens. Conversely, the time variable demonstrates a comparable effect under both coated and uncoated conditions.

Figures 9(c) and 9(d), provide the three-dimensional response surface plots that depict the cumulative impact of the quantitative factors. The findings indicate that the patterns of time and temperature are uniform across both levels of the categorical factor. The MCL initially rises with increasing temperature, then declines, peaking at approximately 95 °C. The MCL exhibits a direct positive correlation with heat-treatment duration, consistently increasing over time and reaching its peak at the longest duration examined.

The interaction plots were analyzed to assess the impact of the resin coating on the response variable. Fig. 9(e), displays the relevant interaction diagrams. The findings demonstrate that at heat treatment temperatures of 70 °C and 95 °C, the presence of the coating correlates with a decrease in the MCL. Conversely, at 120 °C, the MCL of coated specimens rises with prolonged heat treatment duration.

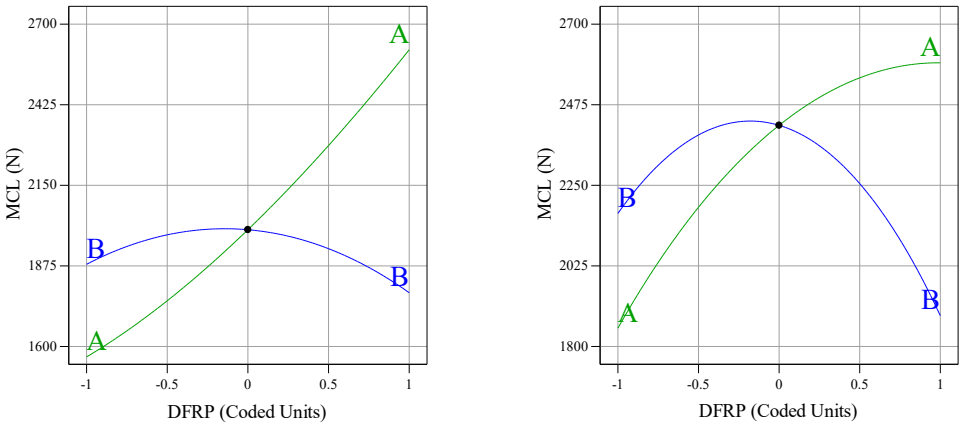
A comparable tendency is noted regarding the connection between temperature and coating. During heat treatment durations of 30 and 60 minutes, the coating adversely impacts the MCL; however, at 90 minutes, the MCL improves with rising temperatures between 70 and 95 °C. The interaction plots in

Fig. 9(e), indicate that the maximum MCL is attained at heat treatment durations near 90 minutes, temperatures ranging from 70 to 95 °C, and under the coated state.

In FFF additive manufacturing, material is deposited through high-temperature extrusion followed by rapid cooling, which typically results in reduced crystallinity and the development of residual thermal stresses. Post-process heat treatment can increase the degree of crystallinity and relieve internal stresses, thereby improving the mechanical performance of the material. The observed increase in the MCL with increasing heat treatment temperature, followed by a decrease at temperatures above approximately 95 °C, can be explained by the thermal transitions of PLA+. When the temperature exceeds the glass transition temperature (Tg = 74.15 °C), enhanced molecular chain mobility promotes structural rearrangement and crystallization, leading to improved mechanical properties, [56, 57]. However, as the temperature approaches and exceeds the crystallization temperature (Tc = 110.25 °C), thermal degradation and morphological instability may occur, resulting in a reduction of MCL, [56-58].

The positive effect of heat-treatment time on mechanical properties is attributed to the progressive development of crystalline regions during prolonged thermal exposure. Nevertheless, excessively long heat-treatment durations may cause over-crystallization or phase instability, which adversely affects mechanical performance, [57, 59].

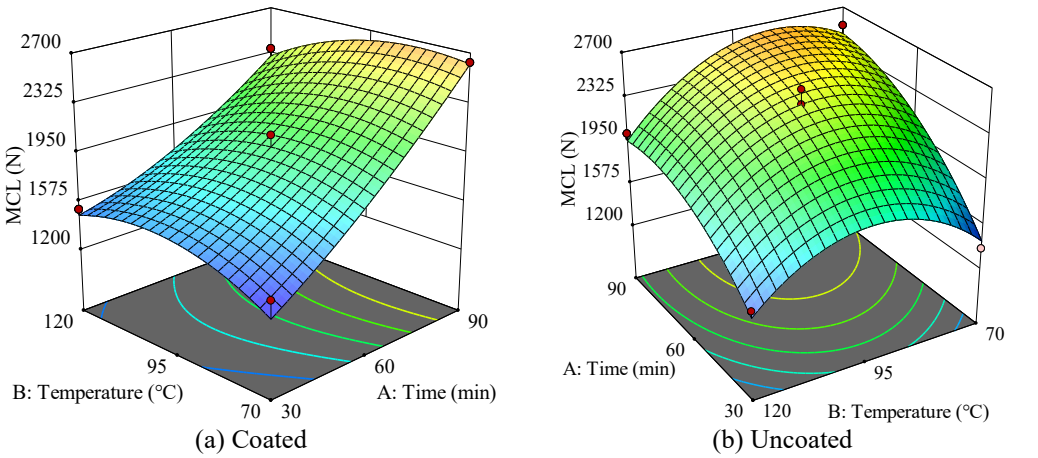
The enhanced MCL observed in coated specimens can be partially attributed to a reduction in surface defect sensitivity. The thin resin coating acts as a barrier to crack initiation and early-stage crack propagation, increasing the energy required for crack growth and thereby improving the load-bearing capacity of the specimens, [42].



(a) Coated (b) Uncoated

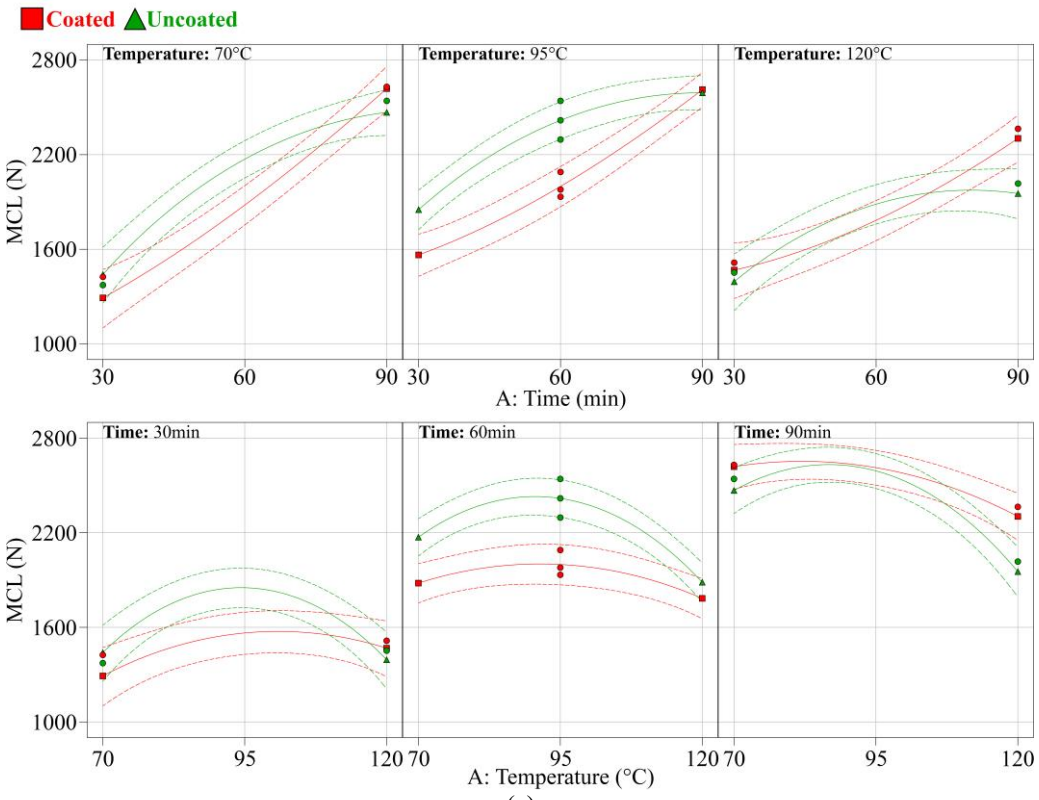
A: Time || B: Temperature || *DFRP: Deviation From Reference Point

Perturbation plots of the response at intermediate values of time and temperature.



(a) Coated (b) Uncoated

Three-dimensional response surface plots illustrating the effects of numeric input variables



(e)

Time–temperature interaction plots including the resin coating factor

Fig. 9 response plots for assessing the effects of input factors

3.2. Optimization of post-processing parameters

Table 6, delineates the ideal post-processing conditions together with the associated response values. The highest point of the response, denoted as the MCL, was attained at a heat-treatment temperature of 82 °C and a duration of 90 minutes. The position of this optimum can be elucidated by the thermal transition characteristics of PLA+. Section 3.1.3 indicates that the optimal heat-treatment window is between 60 and 95 °C, encompassing the glass transition and crystallization phases of the material. The optimal temperature of 82 °C facilitates molecular chain rearrangement and increased crystallinity, resulting in superior mechanical performance, [56-58].

A heat-treatment duration of 90 minutes optimally promotes crystalline formation, therefore augmenting the maximum achievable compressive load under the examined conditions, [57, 59]. The resin coating enhances resistance to crack initiation and early-stage propagation, hence augmenting the load-bearing capability of the specimens, [42].

Table 6 Optimization conditions and their results

Optimization Constraints				
Criteria	Goal	Lower Limit	Upper Limit	Importance
Time (min)		30	90	
Temperature (°C)	in Range	70	120	3
Coating		Coated	Uncoated	
Response				
MCL (N)	Maximize	1334	2874	5

Optimized post-processing condition						
Time (min)	Temperature (°C)	Coating	Desirability (%)	MCL (N)		Error (%)
				Actual	Predicted	
90	80	Coated	84.1	2453	2653	8.15

*Designation of the specimen optimized by topology and post-processing: **Ti90Te82C**

3.3. Comparison of Specimen Optimized by Topology and Post-Processing

3.3.1. Mechanical Properties

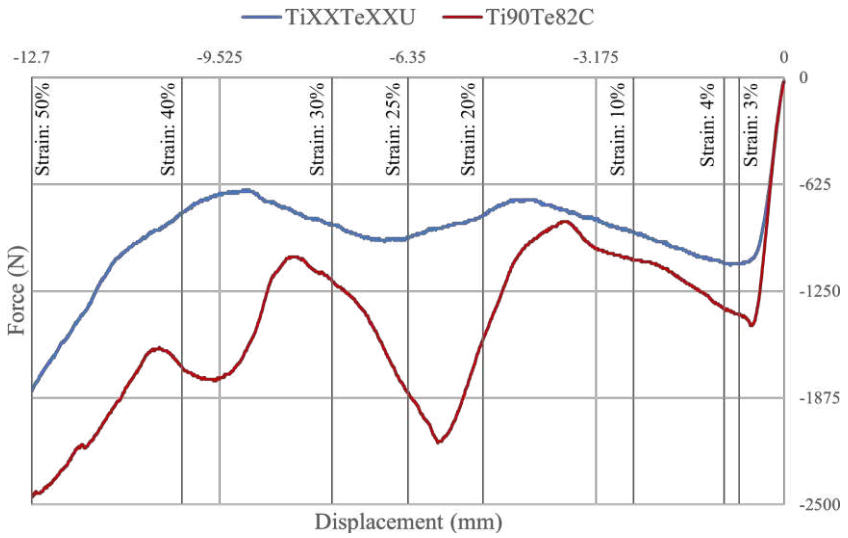
A comparison of specimens Ti90Te82C (topology-optimized and heat-treated) and TiXXTeXXU (topology-optimized only) reveals that the first one demonstrates a 33.75% greater MCL. Table 7 demonstrates that the mass reduction for TiXXTeXXU and Ti90Te82C was 66.14% and 58.50%, respectively. The mass reduction for Ti90Te82C closely aligns with the topology optimization target of 60%, signifying that the optimization goal was achieved with satisfactory precision, resulting in enhanced load-bearing capability during post-processing.

Table 7 Mass variation compared to the standard compression test

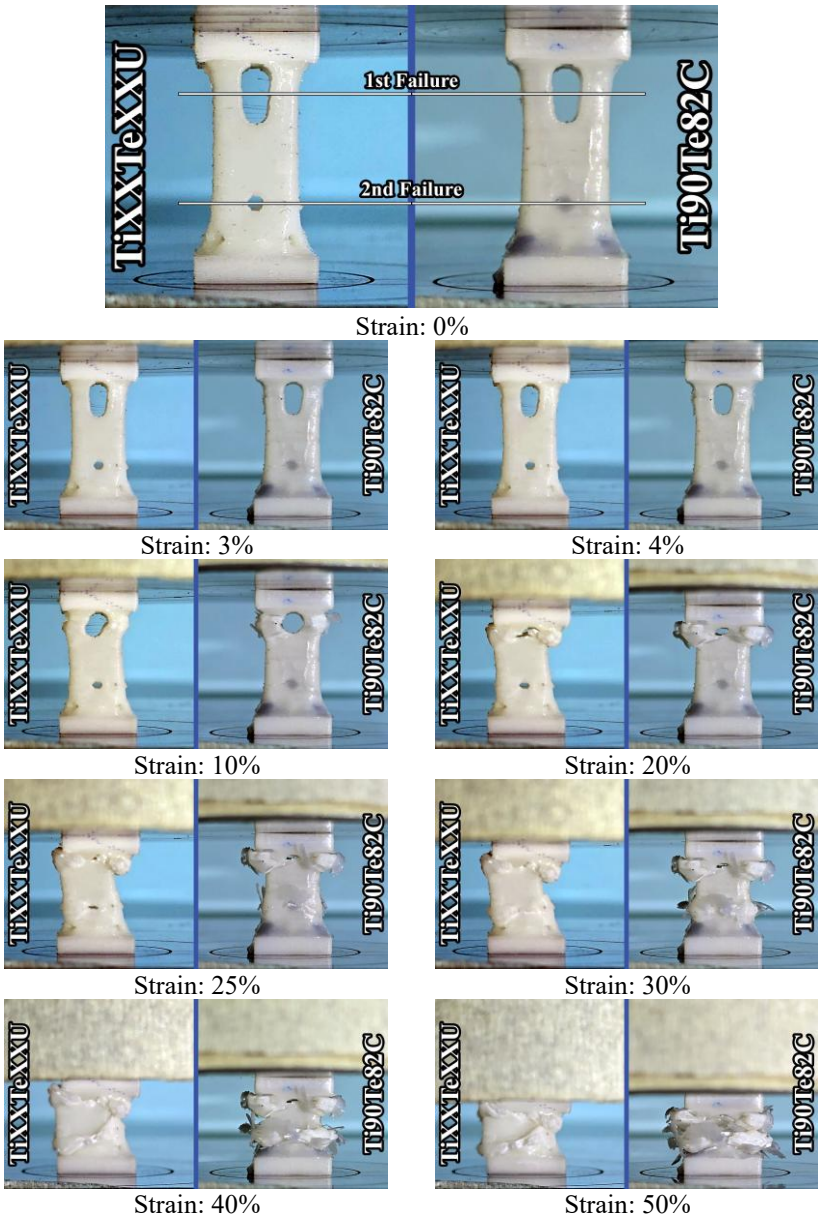
Specimen	Weight (gr)					Average	Variations compared to the standard compression test specimen (%)
Compression test standard specimen	5.18	5.19	5.20	5.18	5.18	5.186	----------
TiXXTeXXU	1.78	1.70	1.74	1.76	1.80	1.756	66.14
Ti90Te82C	2.12	2.16	2.19	2.14	2.15	2.152	58.50

Figure 10(a), displays the force–displacement curves for specimens Ti90Te82C and TiXXTeXXU. Both curves demonstrate a bifurcated failure mechanism marked by two separate load reductions, attributable to the complex topology of the specimens and the existence of localized stress concentrators.

Figure 10(b), displays the specimen image at 0% strain, highlighting the areas that risk failure. Failure commences at areas with diminished cross-sectional dimensions and geometric irregularities; these sites function as stress concentrators, hence dictating the observed two-step collapse.



(a) Force-displacement plot of two specimens Ti90Te82C, and TiXXTeXXU



Strain: 0%

Strain: 3%

Strain: 4%

Strain: 10%

Strain: 20%

Strain: 25%

Strain: 30%

Strain: 40%

Strain: 50%

(b) Visual comparison of Ti90Te82C and TiXXTeXXU specimens

Fig. 10 Comparison of the mechanical properties of Ti90Te82C and TiXXTeXXU

3.3.2. Crystallinity

The XRD analysis indicates a substantial enhancement in crystallinity after heat treatment: Ti90Te82C and TiXXTeXXU exhibit crystallinity indices of 29.25% and 8.81%, respectively, Fig. 11. This corresponds to an absolute increase of 20.44% points and a relative increase of ≈231.9%. Given this marked increase in crystalline fraction, it is reasonable to attribute the observed improvement in MCL of the topology- and post-processed specimen primarily to enhanced PLA+ crystallinity, which promotes higher load-bearing capacity, [56-59].

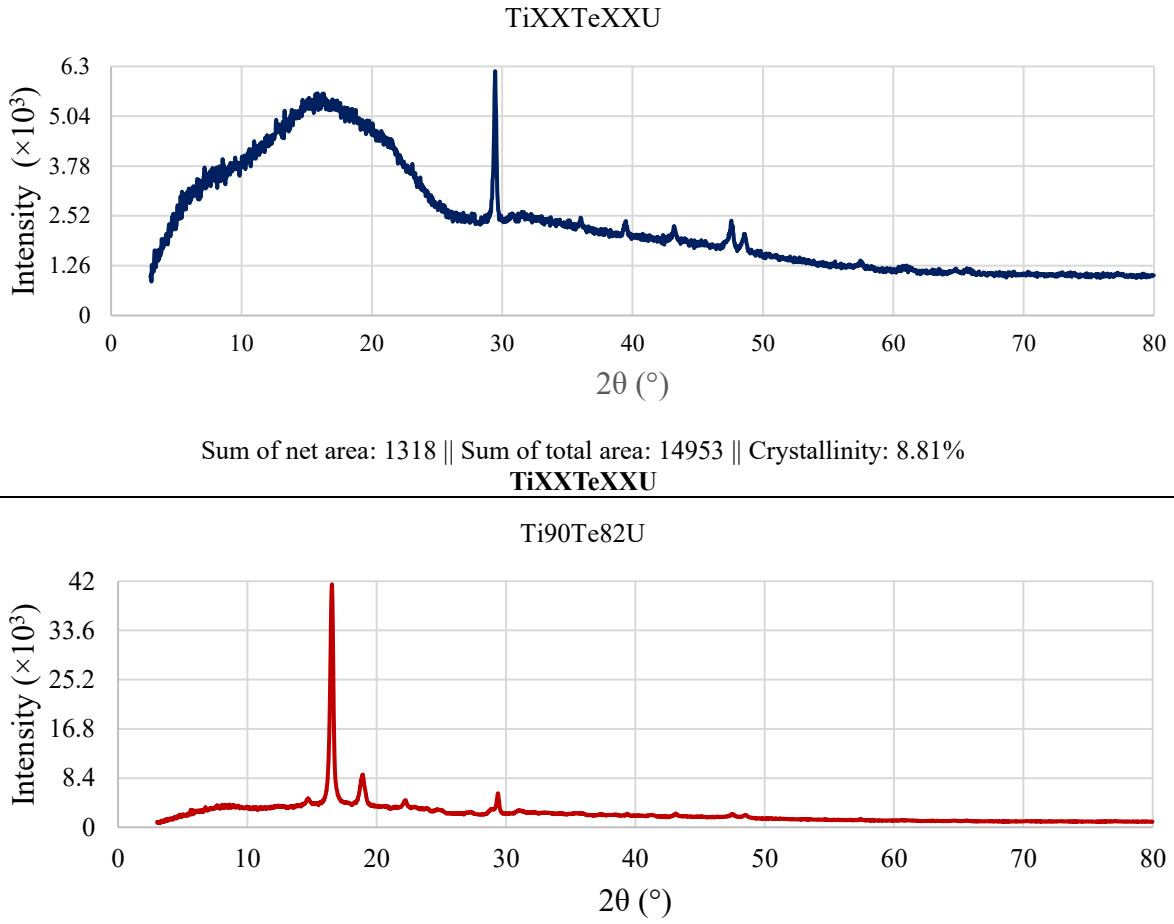


Fig. 11 XRD patterns of the two specimens in the uncoated condition, comparing the specimen subjected to heat treatment with the as-printed specimen.

3.3.3. Resin coating evaluation

Three critical aspects must be considered while evaluating the resin coating, 1- including the thickness of the resin coating. 2- The lack of porosity at the interface between the resin and PLA+. 3- The interface creation between the two materials is contingent upon the surface texture of the sample. FESEM images were obtained from the cross-section of the specimen designated TiXXTeXXC. Fig. 12, displays the photos of the cross-section of the sample fractured by liquid nitrogen. The image analysis was conducted with ImageJ V1.52 software. The figure suggests the average thickness of the resin coating is 0.186 mm, with the resin deposited on the specimen lacking of porosity. The PLA+-resin border has formed without defects, and the resin has conformed to the outer surface texture of the specimen before solidifying.

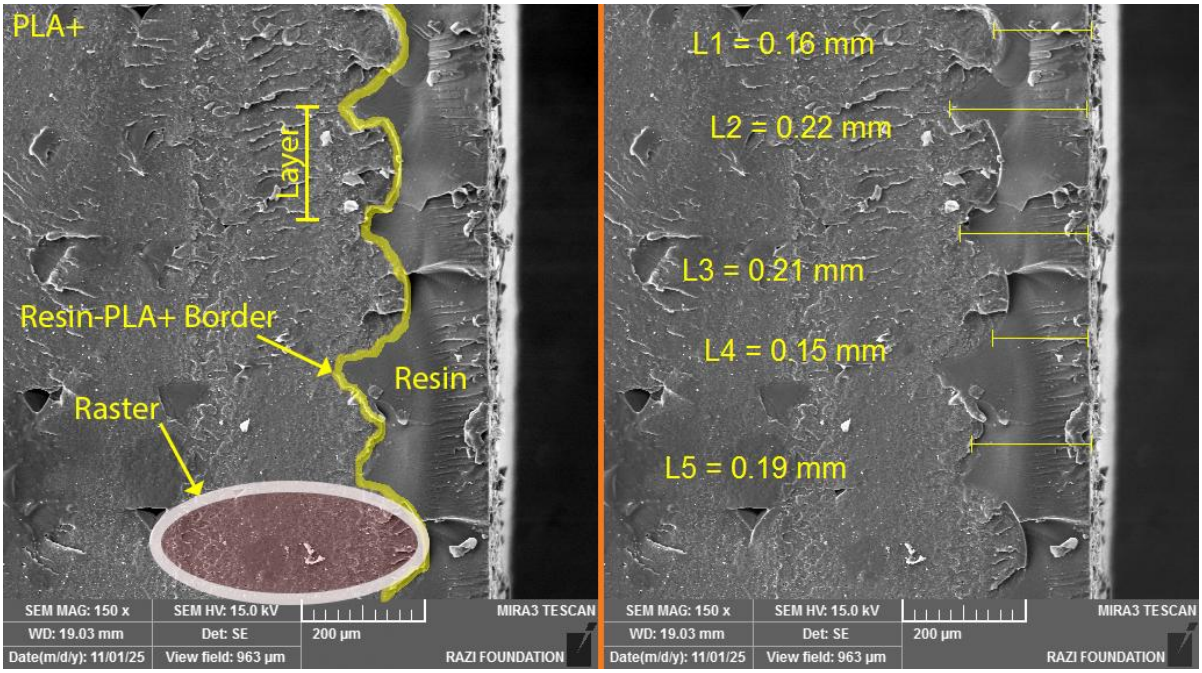


Fig. 12 FESEM images of the coating layer formed on the TiXXTeXXC

4. Conclusion

The present study demonstrates that the integration of topology optimization and post-processing markedly improves the mechanical performance and decreases the bulk of PLA+ components. The principal conclusions are encapsulated as follows:

•Agreement between numerical and experimental findings

FEA demonstrated strong concordance with experimental compression testing, validating the dependability of numerical analysis for assessing the mechanical properties of topology-optimized samples. Due to the geometric complexity of the optimized structures, FEA is the most precise technique for evaluating stress distribution. The SIMP method utilized in this work offered both efficiency and precision, rendering it a feasible strategy for the design of lightweight buildings.

•Influence of heat treatment and coating on MCL

Experimental findings demonstrated that both the duration and temperature of heat treatment significantly impact the MCL of topology-optimized specimens. Excessive temperatures above the glass transition and crystallization temperatures of PLA+ can compromise the molecular structure, resulting in polymer chain degradation. Likewise, prolonged heat treatment reduces crystallinity, negatively impacting mechanical properties. Consequently, choosing a suitable heat treatment period is essential for enhancing load-bearing capacity and durability.

While the effect of coating was less significant than that of heat treatment, it successfully augmented mechanical strength and MCL by impeding crack propagation and improving fracture strain. An optimization of post-processing configurations resulted in an approximate 34% enhancement in MCL.

•Mathematical Modeling

This study presents a prediction model that correctly calculates the MCL of FFF-manufactured, topology-optimized PLA+ components. This model clarifies the impact of post-processing parameters on mechanical performance and allows the adjustment of processing settings to attain maximum strength.

•Analysis of Crystallinity and Microstructure

XRD examination demonstrated that heat treatment improved specimen crystallinity by approximately 232%, underscoring its efficacy in improving stress relief and mechanical properties. Microscopic analysis of the cross-sections of the coated samples demonstrated consistent resin distribution and strong substrate adherence, offering visible proof of the coating's efficacy in enhancing MCL.

Based on these findings, several avenues for future investigation are suggested:

Assessing analogous optimization and post-processing techniques on alternative materials, such as engineering polymers and metals, to extrapolate the findings.

Utilizing optimal compression specimen geometries as unit cells for the design and manufacturing of larger or lightweight structures.

Investigating alternate topology optimization techniques (e.g., BESO, ESO, or metaheuristic algorithms) to enhance design precision.

Examining the impact of various coatings (resin-based, nanostructured, or hybrid) on the mechanical and thermal characteristics of PLA+ components.

Evaluating specimen performance under cyclic loading, fluctuating temperatures, and diverse environmental conditions to ascertain durability and stability in practical applications.

Performing comprehensive microscopic analyses on resin-encased specimens to investigate crack propagation and formulate techniques for fracture prevention.

References

[1] R. Kumar, M. Kumar, and J. S. Chohan, "The role of additive manufacturing for biomedical applications: A critical review," *Journal of Manufacturing Processes,* vol. 64, pp. 828-850, 2021/04/01/ 2021, doi: https://doi.org/10.1016/j.jmapro.2021.02.022.

[2] J. C. Ji, Q. Luo, and K. Ye, "Vibration control based metamaterials and origami structures: A state-of-the-art review," *Mechanical Systems and Signal Processing,* vol. 161, p. 107945, 2021/12/01/ 2021, doi: https://doi.org/10.1016/j.ymssp.2021.107945.

[3] O. Diegel, A. Nordin, and D. Motte, *A practical guide to design for additive manufacturing*. Springer, 2020.

[4] S. H. Siddique, P. J. Hazell, H. Wang, J. P. Escobedo, and A. A. H. Ameri, "Lessons from nature: 3D printed bio-inspired porous structures for impact energy absorption – A review," *Additive Manufacturing,* vol. 58, p. 103051, 2022/10/01/ 2022, doi: https://doi.org/10.1016/j.addma.2022.103051.

[5] N. Jayanth, K. Jaswanthraj, S. Sandeep, N. H. Mallaya, and S. R. Siddharth, "Effect of heat treatment on mechanical properties of 3D printed PLA," *Journal of the Mechanical Behavior of Biomedical Materials,* vol. 123, p. 104764, 2021/11/01/ 2021, doi: https://doi.org/10.1016/j.jmbbm.2021.104764.

[6] J. R. C. Dizon, C. C. L. Gache, H. M. S. Cascolan, L. T. Cancino, and R. C. Advincula, "Post-Processing of 3D-Printed Polymers," *Technologies,* vol. 9, no. 3, 2021, doi: https://doi.org/10.3390/technologies9030061.

[7] L. L. López Taborda *et al.*, "Experimental study of resin coating to improve the impact strength of fused filament fabrication process pieces," *Rapid Prototyping Journal,* vol. 27, no. 3, pp. 475-486, 2021, doi: https://doi.org/10.1108/RPJ-08-2018-0194.

[8] J. Butt and R. Bhaskar, "Investigating the Effects of Annealing on the Mechanical Properties of FFF-Printed Thermoplastics," *Journal of Manufacturing and Materials Processing,* vol. 4, no. 2, 2020, doi: https://doi.org/10.3390/jmmp4020038.

[9] Y. Liao *et al.*, "Erratum: Effect of Porosity and Crystallinity on 3D Printed PLA Properties. Polymers 2019, 11, 1487," *Polymers,* vol. 12, no. 1, 2020, doi: https://doi.org/10.3390/polym12010142.

[10] J. Zhu, H. Zhou, C. Wang, L. Zhou, S. Yuan, and W. Zhang, "A review of topology optimization for additive manufacturing: Status and challenges," *Chinese Journal of Aeronautics,* vol. 34, no. 1, pp. 91-110, 2021/01/01/ 2021, doi: https://doi.org/10.1016/j.cja.2020.09.020.

[11] M. P. Bendsøe and N. Kikuchi, "Generating optimal topologies in structural design using a homogenization method," *Computer Methods in Applied Mechanics and Engineering,* vol. 71, no. 2, pp. 197-224, 1988/11/01/ 1988, doi: https://doi.org/10.1016/0045-7825(88)90086-2.

[12] Y. M. Xie and G. P. Steven, "A simple evolutionary procedure for structural optimization," *Computers & Structures,* vol. 49, no. 5, pp. 885-896, 1993/12/03/ 1993, doi: https://doi.org/10.1016/0045-7949(93)90035-C.

[13] X. Y. Yang, Y. M. Xie, G. P. Steven, and O. M. Querin, "Bidirectional evolutionary method for stiffness optimization," *AIAA journal,* vol. 37, no. 11, pp. 1483-1488, 1999, doi: https://doi.org/10.2514/2.626.

[14] J. H. Zhu, W. H. Zhang, and K. P. Qiu, "Bi-directional evolutionary topology optimization using element replaceable method," *Computational Mechanics,* vol. 40, pp. 97-109, 2007, doi: https://doi.org/10.1007/s00466-006-0087-0.

[15] O. M. Querin, V. Young, G. P. Steven, and Y. M. Xie, "Computational efficiency and validation of bi-directional evolutionary structural optimisation," *Computer Methods in Applied Mechanics and Engineering,* vol. 189, no. 2, pp. 559-573, 2000/09/01/ 2000, doi: https://doi.org/10.1016/S0045-7825(99)00309-6.

[16] X. Huang and Y. M. Xie, "Convergent and mesh-independent solutions for the bi-directional evolutionary structural optimization method," *Finite Elements in Analysis and Design,* vol. 43, no. 14, pp. 1039-1049, 2007/10/01/ 2007, doi: https://doi.org/10.1016/j.finel.2007.06.006.
[17] G. I. N. Rozvany, M. Zhou, and T. Birker, "Generalized shape optimization without homogenization," *Structural optimization,* vol. 4, no. 3, pp. 250-252, 1992/09/01 1992, doi: https://doi.org/10.1007/BF01742754.
[18] "SIMP Method for Topology Optimization." SOLIDWORKS. https://help.solidworks.com/2024/english/SolidWorks/cworks/c_simp_method_topology.htm?verRedirect=1 (accessed 2024).
[19] S. Belhabib and S. Guessasma, "Compression performance of hollow structures: From topology optimisation to design 3D printing," *International Journal of Mechanical Sciences,* vol. 133, pp. 728-739, 2017/11/01/ 2017, doi: https://doi.org/10.1016/j.ijmecsci.2017.09.033.
[20] Y.-F. Fu, B. Rolfe, L. N. S. Chiu, Y. Wang, X. Huang, and K. Ghabraie, "Design and experimental validation of self-supporting topologies for additive manufacturing," *Virtual and Physical Prototyping,* vol. 14, no. 4, pp. 382-394, 2019, doi: https://doi.org/10.1080/17452759.2019.1637023.
[21] J. Dvorakova and K. Dvorak, "Topological optimization of a component made by the FDM method," *Int. J. Mech. Eng. Robot. Res,* vol. 10, no. 2, pp. 67-71, 2021, doi: https://doi.org/10.18178/ijmerr.10.2.67-71.
[22] I. Antar, M. Othmani, K. Zarbane, M. El Oumami, and Z. Beidouri, "Topology optimization of a 3D part virtually printed by FDM," *Journal of Achievements in Materials and Manufacturing Engineering,* vol. 112, no. 1, 2022, doi: http://dx.doi.org/10.5604/01.3001.0016.0289.
[23] S. Brischetto and R. Torre, "Tensile and Compressive Behavior in the Experimental Tests for PLA Specimens Produced via Fused Deposition Modelling Technique," *Journal of Composites Science*, vol. 4, no. 3, doi: https://doi.org/10.3390/jcs4030140.
[24] J. Giri, A. Chiwande, Y. Gupta, C. Mahatme, and P. Giri, "Effect of process parameters on mechanical properties of 3d printed samples using FDM process," *Materials Today: Proceedings,* vol. 47, pp. 5856-5861, 2021, doi: https://doi.org/10.1016/j.matpr.2021.04.283.
[25] P. Geng *et al.*, "Effects of printing parameters on the mechanical properties of high-performance polyphenylene sulfide three-dimensional printing," *3D Printing and Additive Manufacturing,* vol. 8, no. 1, pp. 33-41, 2021, doi: https://doi.org/10.1089/3dp.2020.0052.
[26] P. Yadav, A. Sahai, and R. S. Sharma, "Strength and Surface Characteristics of FDM-Based 3D Printed PLA Parts for Multiple Infill Design Patterns," *Journal of The Institution of Engineers (India): Series C,* vol. 102, no. 1, pp. 197-207, 2021/02/01 2021, doi: https://doi.org/10.1007/s40032-020-00625-z.
[27] G. Y. Dakhil, R. M. Salih, and A. M. Hameed, "Influence of infill pattern, infill ratio on compressive strength and hardness of 3D printed polylactic acid (PLA) based polymer," *Journal of Applied Sciences and Nanotechnology,* vol. 3, no. 1, pp. 1-7, 2023, doi: https://doi.org/10.53293/jasn.2022.4745.1141.
[28] K. Özsoy, A. Erçetin, and Z. A. Çevik, "Comparison of mechanical properties of PLA and ABS based structures produced by fused deposition modelling additive manufacturing," *Avrupa Bilim ve Teknoloji Dergisi,* no. 27, pp. 802-809, 2021, doi: https://doi.org/10.31590/ejosat.983317.
[29] N. Beattie, N. Bock, T. Anderson, T. Edgeworth, T. Kloss, and J. Swanson, "Effects of build orientation on mechanical properties of fused deposition modeling parts," *Journal of Materials Engineering and Performance,* vol. 30, pp. 5059-5065, 2021, doi: https://doi.org/10.1007/s11665-021-05624-4.
[30] K. N. Gunasekaran, V. Aravinth, C. B. Muthu Kumaran, K. Madhankumar, and S. Pradeep Kumar, "Investigation of mechanical properties of PLA printed materials under varying infill density," *Materials Today: Proceedings,* vol. 45, pp. 1849-1856, 2021/01/01/ 2021, doi: https://doi.org/10.1016/j.matpr.2020.09.041.

[31] M. Heidari-Rarani, N. Ezati, P. Sadeghi, and M. R. Badrossamay, "Optimization of FDM process parameters for tensile properties of polylactic acid specimens using Taguchi design of experiment method," *Journal of Thermoplastic Composite Materials,* vol. 35, no. 12, pp. 2435-2452, 2022/12/01 2020, doi: https://doi.org/10.1177/0892705720964560.

[32] R. Srinivasan, T. Pridhar, L. S. Ramprasath, N. S. Charan, and W. Ruban, "Prediction of tensile strength in FDM printed ABS parts using response surface methodology (RSM)," *Materials Today: Proceedings,* vol. 27, pp. 1827-1832, 2020/01/01/ 2020, doi: https://doi.org/10.1016/j.matpr.2020.03.788.

[33] M. S. Saad, A. Mohd Nor, M. Z. Zakaria, M. E. Baharudin, and W. S. Yusoff, "Modelling and evolutionary computation optimization on FDM process for flexural strength using integrated approach RSM and PSO," *Progress in Additive Manufacturing,* vol. 6, no. 1, pp. 143-154, 2021/02/01 2021, doi: https://doi.org/10.1007/s40964-020-00157-z.

[34] M. Vorkapić, I. Mladenović, M. Pergal, T. Ivanov, and M. Baltić, "Optimisation of tensile stress of poly (lactic acid) 3D printed materials using response surface methodology," *Tribology and Materials,* vol. 1, no. 2, pp. 70-80, 2022, doi: https://doi.org/10.46793/tribomat.2022.009.

[35] J.-H. Hong, T. Yu, Z. Chen, S.-J. Park, and Y.-H. Kim, "Improvement of flexural strength and compressive strength by heat treatment of PLA filament for 3D-printing," *Modern Physics Letters B,* vol. 33, no. 14n15, p. 1940025, 2019, doi: https://doi.org/10.1142/S0217984919400256.

[36] P. Gupta, S. Kumari, A. Gupta, A. K. Sinha, and P. Jindal, "Effect of heat treatment on mechanical properties of 3D printed polylactic acid parts," vol. 63, no. 1, pp. 73-78, 2021, doi: https://doi.org/10.1515/mt-2020-0010.

[37] R. V. Pazhamannil, N. Krishnan C, G. P, and A. Edacherian, "Investigations into the effect of thermal annealing on fused filament fabrication process," *Advances in Materials and Processing Technologies,* vol. 8, no. sup2, pp. 710-723, 2022, doi: https://doi.org/10.1080/2374068X.2021.1946753.

[38] M. Shbanah, M. Jordanov, Z. Nyikes, L. Tóth, and T. A. Kovács, "The Effect of Heat Treatment on a 3D-Printed PLA Polymer's Mechanical Properties," *Polymers*, vol. 15, no. 6, doi: https://doi.org/10.3390/polym15061587.

[39] F. Kartal and A. Kaptan, "Effects of annealing temperature and duration on mechanical properties of PLA plastics produced by 3D Printing," (in en), *European Mechanical Science,* vol. 7, no. 3, pp. 152-159, September 2023, doi: https://doi.org/10.26701/ems.1290961.

[40] W. Yu, X. Wang, X. Yin, E. Ferraris, and J. Zhang, "The effects of thermal annealing on the performance of material extrusion 3D printed polymer parts," *Materials & Design,* vol. 226, p. 111687, 2023/02/01/ 2023, doi: https://doi.org/10.1016/j.matdes.2023.111687.

[41] P. Janmanee and P. Ratchapakdee, "Effect of Annealing on Tensile Strength of 3D Printed PLA with Material Extrusion," *Mechanics of Advanced Composite Structures,* 2024, doi: https://doi.org/10.22075/macs.2024.33892.1662.

[42] S. Barone, P. Neri, S. Orsi, A. Paoli, A. V. Razionale, and F. Tamburrino, "Two coatings that enhance mechanical properties of fused filament-fabricated carbon-fiber reinforced composites," *Additive Manufacturing,* vol. 32, p. 101105, 2020/03/01/ 2020, doi: https://doi.org/10.1016/j.addma.2020.101105.

[43] H. Koçak, "Surface Modification of a Model Part Produced with 3D Printing from PLA Material by Means of Composite Coating," *Journal of Materials Engineering and Performance,* vol. 30, no. 5, pp. 3903-3910, 2021/05/01 2021, doi: https://doi.org/10.1007/s11665-021-05711-6.

[44] R. Kumar, M. Kumar, J. S. Chohan, N. K. Singh, and D. K. Mahajan, "Corrosion and Thermal Analysis of 316L Stainless Steel Coated PLA Parts Fabricated by FDM Process for Biomedical Applications," *Protection of Metals and Physical Chemistry of Surfaces,* vol. 59, no. 4, pp. 736-749, 2023/08/01 2023, doi: https://doi.org/10.1134/S2070205123700661.

[45] P. Satyanarayana, Y. S. Narayan, K. J. Prakash, J. Cherukuri, and D. Maneiah, "Investigating The Surface Characteristics of Dip Coated 3D Printed ABS Specimens," *International Journal of Integrated Engineering,* vol. 15, no. 5, pp. 41-54, 2023, doi: https://doi.org/10.30880/ijie.2023.15.05.006.
[46] A. Chiocca, F. Tamburrino, F. Frendo, and A. Paoli, "Effects of coating on the fatigue endurance of FDM lattice structures," *Procedia Structural Integrity,* vol. 42, pp. 799-805, 2022/01/01/ 2022, doi: https://doi.org/10.1016/j.prostr.2022.12.101.
[47] "eSUN PLA+ filament." https://www.esun3d.com/pla-pro-product/ (accessed.
[48] A. Gaweł, S. Kuciel, A. Liber-Kneć, and D. Mierzwiński, "Examination of Low-Cyclic Fatigue Tests and Poisson's Ratio Depending on the Different Infill Density of Polylactide (PLA) Produced by the Fused Deposition Modeling Method," *Polymers,* vol. 15, no. 7, p. 1651, 2023, doi: https://doi.org/10.3390/polym15071651.
[49] "Anycubic Resin User Manual & MSDS." https://store.anycubic.com/pages/resin-user-manual (accessed.
[50] M. Serge, T. Patrick, and F. Duquenoy, "Chapter 6 - Motion Systems: An Overview of Linear, Air Bearing, and Piezo Stages," in *Three-Dimensional Microfabrication Using Two-photon Polymerization*, T. Baldacchini Ed. Oxford: William Andrew Publishing, 2016, pp. 148-167.
[51] R. M. Smith and C. Plackner, "The family approach to assessing fit in Rasch measurement," *Journal of Applied Measurement,* vol. 10, no. 4, pp. 424-437, 2009.
[52] D. I. MacKenzie, J. D. Nichols, J. A. Royle, K. H. Pollock, L. L. Bailey, and J. E. Hines, "Chapter 3 - Fundamental Principals of Statistical Inference," in *Occupancy estimation and modeling*: Elsevier, 2018, pp. 71-111.
[53] "ANOVA Output." https://www.statease.com/docs/latest/contents/analysis/anova-output/ (accessed.
[54] S. Weisberg, *Applied linear regression*. John Wiley & Sons, 2005.
[55] V. Bagdonavičius and L. Petkevičius, "A new multiple outliers identification method in linear regression," *Metrika,* vol. 83, no. 3, pp. 275-296, 2020, doi: https://doi.org/10.1007/s00184-019-00731-8.
[56] R. V. Pazhamannil, P. Govindan, A. Edacherian, and H. M. Hadidi, "Impact of process parameters and heat treatment on fused filament fabricated PLA and PLA-CF," *International Journal on Interactive Design and Manufacturing (IJIDeM),* vol. 18, no. 4, pp. 2199-2213, 2024/05/01 2024, doi: https://doi.org/10.1007/s12008-022-01082-x.
[57] Ç. Kahya, O. Tunçel, O. Çavuşoğlu, and K. Tüfekci, "Thermal annealing optimization for improved mechanical performance of PLA parts produced via 3D printing," *Polymer Testing,* vol. 144, p. 108735, 2025/03/01/ 2025, doi: https://doi.org/10.1016/j.polymertesting.2025.108735.
[58] O. Mysiukiewicz and M. Barczewski, "Crystallization of polylactide-based green composites filled with oil-rich waste fillers," *Journal of Polymer Research,* vol. 27, no. 12, p. 374, 2020/11/18 2020, doi: https://doi.org/10.1007/s10965-020-02337-5.
[59] X. Liu, X. Hua, and H. Wu, "Degradation Behavior of Poly (Lactic Acid) during Accelerated Photo-Oxidation: Insights into Structural Evolution and Mechanical Properties," *Journal of Polymers and the Environment,* vol. 32, no. 8, pp. 3810-3821, 2024/08/01 2024, doi: https://doi.org/10.1007/s10924-024-03211-x.